Egypt. J. Microbiol. **Vol. 57,** pp. 15-34 (2022)

EgyptianJournalofMicrobiology
http://ejm.journals.ekb.eg/

Synthesis, Characterization, and Antimicrobial Activities of $Cu_xFe_{3-x}O_4$/PANI Nanocomposites

Mohammed A. Eid[(1)#], Abeer A. El-Helaly[(2)], Mohamed Y. El-Sheikh[(2)], Hosny A. El-Daly[(2)], Ali H. Gemeay[(2)]

[(1)]Botany and Microbiology Department, Faculty of Science, Tanta University, Tanta, Egypt; [(2)]Chemistry Department, Faculty of Science, Tanta University, Tanta, Egypt.

MAGNETIC nanocomposites loaded with antimicrobial drugs have grown in popularity for treating infectious diseases due to their magnetic properties and the ability to penetrate bacteria cells. In this research, $Cu_xFe_{3-x}O_4$ nanoparticles and $Cu_xFe_{3-x}O_4$/PANI nanocomposites were synthesized, characterized, and examined for their antimicrobial activity. The in-situ oxidative polymerization of aniline in the presence of $Cu_xFe_{3-x}O_4$ nanoparticles produced $Cu_xFe_{3-x}O_4$/PANI nanocomposites with distinct spinel ferrites. XRD, FT-IR, VSM, SEM, EDX, TEM, and XPS techniques confirmed the successful synthesis of the $Cu_xFe_{3-x}O_4$/PANI nanocomposites. The analysis of magnetization patterns of $Cu_xFe_{3-x}O_4$/PANI nanocomposites revealed their superparamagnetic characteristics. With increasing Cu^{2+} ratios, both the pure copper ferrites nanoparticles and the $Cu_xFe_{3-x}O_4$/PANI nanocomposites exhibited enhanced antimicrobial effects against gram-positive (*Staph*), gram-negative (*E. coli, P. aeruginosa*, and *K. pneumoniae*), and fungi such as (*C. albicans*), which is consistent with decreasing the order of crystal size (nm) and the lattice strain, where crystal size and lattice strain decreased with increasing Cu^{2+} ratio. SEM micrographs revealed changes in bacterial shape, deformation of fungal cell walls, and bacterial and yeast colonies collapsing. Furthermore, the nanocomposites are more effective against gram-negative bacteria and *Candida albicans* than gram-positive bacteria, displaying the alteration of bacterial shape, fungal cell wall deformation, and collapsing bacterial and yeast colonies. The results presented an approach for using $Cu_xFe_{3-x}O_4$ and $Cu_xFe_{3-x}O_4$/PANI as an alternative promising antimicrobial agent against several multidrug-resistant microbes.

Keywords: Antimicrobial, *Candida albicans*, $Cu_xFe_{3-x}O_4$/PANI nanocomposites, Gram-negative bacteria, Gram-positive bacteria.

Introduction

Magnetic nanoparticles have attracted much interest in biomedicine because of their beneficial magnetic, optical, and antibacterial properties (Gheidari et al., 2020). Spinel ferrites with remarkable electrical and magnetic properties and outstanding chemical stability received much attention (Hegazy et al., 2018). Based on these properties, a variety of applications have been reported, including medical (Amiri et al., 2019b; Predoi et al., 2019), immunoassay (Wu et al., 2020), electronic devices (Qindeel et al., 2021), adsorption (Predoi et al., 2020), and catalysis (Amiri et al., 2019a). Spinel ferrites have three well-known structures: normal, inverse, and mixed spinel ferrites, based on the +2 and +3 cations distribution in the crystal lattice, where Fe^{3+} ions occupy the octahedral sites in normal spinel ferrite, while the M^{2+} ions occupy the tetrahedral sites. $CuFe_2O_4$ can form either an inverse or mixed spinel structure depending on the synthesis conditions (Masunga et al., 2019). The distribution of Fe^{3+} ions on the tetrahedral (A) and octahedral (B) sites has been reported (Mulud et al., 2020) such as $(Cu^{2+}_{0.8}Fe^{3+}_{0.2})_A (Cu^{3+}_{0.2}Fe^{2+}_{0.2}Fe^{3+}_{1.6})_B O_4$ (Rajput et al., 2015; Ghaani & Saffari, 2016). Copper

#Corresponding author email: mohamed.eid@science.tanta.edu.eg
Received: 13/02/2022; Accepted: 03/07/2022
DOI: 10.21608/EJM.2022.116185.1206

ferrite nanoparticles with excellent electrical properties, regular spinel structure, thermal stability, and narrow bandgap (Masunga et al., 2019) found a variety of applications, including wastewater treatment as a photocatalyst or adsorbent, biomedical applications, rechargeable batteries, gas sensors, and catalysis (Kefeni et al., 2017). Various synthetic processes such as co-precipitation (Salavati-Niasari et al., 2012; Prodan et al., 2013b), combustion (Liu et al., 2009), sol-gel (Sang et al., 2021), solvothermal and hydrothermal processes (Kurian et al., 2021), thermal treatment (Zakiyah et al., 2015), high energy ball milling (Goya et al., 1998), microemulsion (Rashad et al., 2015), solid-state reaction (Tasca et al., 2011), polyol route (Altincekic et al., 2010), microwave-assisted hydrothermal (Sinfrônio et al., 2018), and mechanochemical (Manova et al., 2011) have been mentioned for the preparation of copper ferrites nanoparticles.

Generally, mixing of conducting polymers with metal oxides was utilized to create nanocomposites with reasonable antibacterial properties (Liu et al., 2015). Polyaniline (PANI) prompted great interest in various applications due to its cheap cost, biocompatibility stability, and nontoxicity. Furthermore, PANI has significant limitations, including poor processability and mechanical stability (Ates, 2011). It was established that the interface between the organic polymer and the ferrite nanoparticles utilized the properties of each component and incorporated new properties (Chudobova et al., 2015; Kharazi et al., 2019). The antibacterial activity of cationic polymers involves the electrostatic interactions with bacterial membrane and interfering with their activity. Following this initial electrostatic adhesion, PANI may partially permeate the bacterial membrane and interact with other intracellular biomolecules. In addition, the interaction of magnetite nanoparticles with bacterial cell membrane, in particular, caused membrane disruption and bacterial inactivation, resulting in antibacterial activity. Furthermore, reactive oxygen species (ROS) produced on the microbe surface depolarize bacterial membranes, resulting in oxidative stress and cell membrane damage (Arakha et al., 2015). Moreover, the antimicrobial activity of copper ions against *Salmonella enterica, Campylobacter jejuni, E. coli, Listeria monocytogenes,* and *Staphylococcus aureus* has been reported in several studies (Pham & Lee, 2014).

In this work, $Cu_xFe_{3-x}O_4$ nanoparticles and $Cu_xFe_{3-x}O_4$/PANI nanocomposites were synthesized via co-precipitation followed by in situ oxidative polymerization of aniline. The prepared samples were investigated by sophisticated techniques. After that, the antimicrobial activity of the nanocomposites combined with the benefits of both $Cu_xFe_{3-x}O_4$ and PANI were examined. The antimicrobial activities against various microbes such as *Staphylococcus aureus, Escherichia coli, Pseudomonas aeruginosa, Klebsiella pneumoniae,* and *Candida albicans* have been studied.

Materials and Methods

Chemicals and reagents

Aniline (Across) was distilled before ferrous sulfate anhydrous ($FeSO_4$), ferrous chloride hexahydrate ($FeCl_3.6H_2O$), copper chloride ($CuCl_2$), sodium hydroxide, ethanol, potassium persulfate, $K_2S_2O_8$ (KPS), and hydrochloric acid (35%) were of analytical grade and used without purification. Distilled water was used throughout the experimental work.

Synthesis of $Cu_xFe_{3-x}O_4$ nanoparticles

Copper ferrites ($Cu_xFe_{3-x}O_4$) nanoparticles, where x= 0, 0.1, 0.5, 1.0, were synthesized by co-precipitation procedure using NaOH as the precipitating agent (Gemeay et al., 2020). Briefly, (0.09mol/L) of $FeCl_3.6H_2O$ and (0.045mol/L) of $CuCl_2$ were mixed with the molar ratio of 1: 2 of Cu^{+2}: Fe^{+3} and 0.5 mol/L of NaOH were added drop-wise while being continuously stirred (pH was about 11). Immediately, the brown precipitate was formed with a strong magnetic response, stirring for 2h at 70°C. Before separation, the mixture was allowed to cool to room temperature. After that, it was washed several times with distilled water. The precipitates were re-dispersed using an ultrasonic bath to extract the adsorbed ions and finally dried in an oven at 60°C for 24h. The prepared samples were abbreviated as Cu_0F, $Cu_{0.1}F$, $Cu_{0.5}F$, and $Cu_{1.0}F$.

Synthesis of $Cu_xFe_{3-x}O_4$/PANI nanocomposites

$Cu_xFe_{3-x}O_4$/PANI nanocomposites with various compositions were prepared via in-situ oxidation polymerization of aniline in acidic solution using $K_2S_2O_8$ as an oxidant and different molar ratios of $Cu_xFe_{3-x}O_4$ (x= 0.1, 0.5, 1.0). In brief, 5g of $Cu_xFe_{3-x}O_4$ was dispersed in 250mL of 0.3mol/L HCL solution, followed by added 5.93g

of $K_2S_2O_8$ and then 2mL of aniline was added and stirred for 12h at room temperature. The resulting $Cu_xFe_{3-x}O_4$/PANI nanocomposites were filtered, washed several times with water, finally with ethanol, and dried at 50 °C overnight. The $Cu_xFe_{3-x}O_4$/PANI samples were abbreviated as $Cu_{0.1}$FP, $Cu_{0.5}$FP, and $Cu_{1.0}$FP (Scheme 1).

Instrumentation

X-ray diffraction was used to characterize the synthesized nanocomposites using an automated X-ray diffractometer (X-PERT PRO Philips System) with CuK radiation (λ= 1.54056 Å) of 40kV and 30mA with 2Θ= 2–80° range. FT-IR spectra with KBr were examined in the range of 4000–200 cm^{-1} using JASCO FT-IR-4100 (Japan) spectrometer. The morphology and particle size of the prepared nanocomposites were investigated using a JEM 2100 (JEOL, Japan) electron microscope at an applied potential voltage of 200kV and a scanning electron microscope (SEM) with an FEI Quanta 250 FEG SEM at 10 to 15 kV. The magnetic characteristics of the as-prepared samples were determined using a handmade vibrating sample magnetometer (VSM, Tanta, Egypt) (Araújo et al., 2019). EDX (Rontec, M-series EDR288/SPU2) was used to analyze the elemental composition of the prepared nanocomposites. X-ray photoelectron spectroscopy (XPS) was collected on K-ALPHA (Thermo Fisher Scientific, USA) with monochromatic Al K-alpha radiation from 0 to 1350eV, the spot size of 400 μm at a pressure of 10–9 mbar, with a full spectrum pass energy of 200eV and a narrow spectrum of 50 eV.

Microbes' selection and preparation

Four bacterial strains, one gram-positive (*Staphylococcus aureus*) and three gram-negative (*Escherichia coli*, *Pseudomonas aeruginosa*, and *Klebsiella pneumoniae),* besides one fungal isolate (*Candida albicans),* were selected for the antimicrobial activity tests. These microorganisms were kindly provided by the Bacteriology and Mycology Sections, Botany and Microbiology Department, Faculty of Science, Tanta University, Tanta, Egypt.

$Cu_xFe_{3-x}O_4$ NPs and $Cu_xFe_{3-x}O_4$/PANI nanocomposite antimicrobial activity

The antibacterial activity of $Cu_xFe_{3-x}O_4$ and $Cu_xFe_{3-x}O_4$/PANI nanocomposites was examined using bacteria and fungi cultivated on nutritious agar media. In sterile Petri dishes, the media was placed and allowed to solidify at room temperature. The organisms were placed on top of solidified media, and a suitable number of wells were prepared on each plate. 100μL of $Cu_xFe_{3-x}O_4$ NPs and $Cu_xFe_{3-x}O_4$/PANI nanocomposites suspension ($5x10^{-4}$mg/mL) were added to each well. The plates were incubated for 24h at 30°C. The inhibition zone (mm) for each pathogen was assessed. Ciprofloxacin (5mcg/disc) was used as a positive control. When an area of inhibition encircling the well was identified, the test result was pronounced positive (Table 2).

Results and Discussion

Characterization methods

XRD studies

The X-ray powder diffraction (XRD) patterns of free PANI, Cu_0F, $Cu_{0.5}$F, $Cu_{0.1}$FP, $Cu_{0.5}$FP, and $Cu_{1.0}$FP nanocomposites are shown in Fig. 1. The PANI characteristic peaks at 2Θ= 11.05°, 12.99°, 16.6°, and 19.15° could be attributed to the parallel structure periodically interlaced with the vertical in the polymer chains (Zeng et al., 2016). Peaks at 2Θ= 18.4°, 31.5°, 35.7°, 43.3°, 54.40°, 57.34°, and 63.03° corresponded to (h k l) values of 111, 220, 311, 400, 422, 511, and 440, indicating the presence of single-phase $CuFe_2O_4$ with good crystallinity (JCPDS file No: 25-0283) (Science & Kumar, 2019). The average crystallite size (*D*) was determined using Debye–Scherrer equation as follows: Eq. (1)

$$D= (0.9\ \lambda)/(\beta \cos \theta) \quad (1)$$

where λ= 1.542Å and θ are the Bragg's angle and β full width at half maximum, respectively, of the most intense peak (311), crystal size increased from 6.82 nm in the absence of PANI to 10.95 nm in the presence of PANI. This variation can be ascribed to the aggregation of ferrite nanoparticles after PANI deposition. Furthermore, Table 1 presents some other characteristic parameters calculated from XRD patterns. Based on XRD results, the crystallite size of $CuFe_2O_4$ particles is in the nano-range, which agrees with TEM data in Table 1. The variation of the crystallite size (D), lattice constant (a), d spacing (nm), D_x, lattice strain (ε), L_{A-A}, L_{B-B}, and L_{A-B} (Å) of $Cu_{0.1}$FP, $Cu_{0.5}$FP, $Cu_{1.0}$FP, $Cu_{0.5}$F, and Cu_0F nanocomposites are displayed in Table 1. The values of lattice constant *a* for all samples were determined from the (311) peak using Eq. (2) (Dhiman et al., 2008).

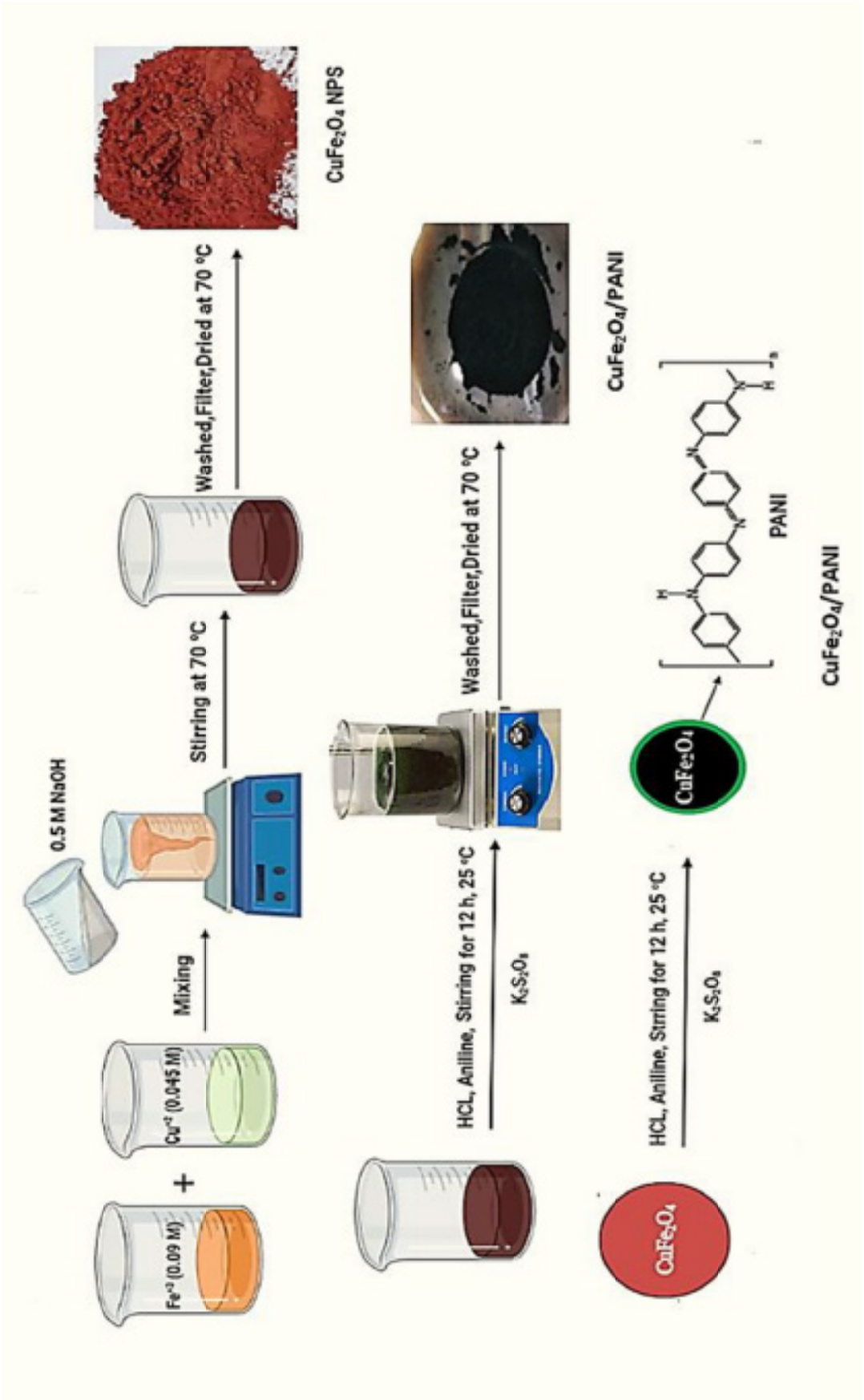

Scheme 1. Graphical representation of $CuFe_2O_4$/PANI nanocomposites

$$a = d\sqrt{(h^2 + k^2 + l^2)} \quad (2)$$

where *h*, *k*, and *l* are the Miller indices, and *d* is the interatomic spacing, the values of *a* are listed in Table 1 and are found to increase from 7.46 to 8.64 Å with an increase of Cu^{2+} ratio (*x*). This is due to the increase in the ionic radius of Cu^{+2}, which indicates that Cu^{2+} has been incorporated into the spinel structure (Ameen Ramiza et al., 2016). Moreover, the calculated lattice constant value of Fe_3O_4 was 8.301Å corresponds to the lattice constant of magnetite (8.384 Å) (Sundrarajan & Ramalakshmi, 2012). The constant lattice value of $CuFe_2O_4$ was 8.357Å, close to the previously reported values (Ali et al., 2020). For the cubic spinel structure, *d*, *a*, and the Miller indices of the reflecting planes (h k l) are calculated from Eq (3):

$$d = \frac{a}{(h^2+k^2+l^2)^{1/2}} \quad (3)$$

Table 1 shows the calculated *a* and *d* values. The observed and calculated *d* values are in good agreement for all samples (Shedam et al., 2016). The X-ray density (D_x) of $Cu_{0.5}F$ and Cu_0F was calculated using Eq. (4) (Saafan et al., 2021):

$$D_x = 8M/(Na^3) \quad (4)$$

where *M* is the molecular weight, *N* is Avogadro's number, and *a* is the lattice constant of the spinel ferrite. The calculated d_x values were 5.4425 and 5.5541g/cm^3 for $Cu_{0.5}F$ and Cu_0F samples, respectively. Moreover, the observed X-ray density (D_x) has quite reasonable values in agreement with the literature (Assar et al., 2015). Furthermore, the average strain of samples was calculated, Eq. (5) (Rather et al., 2021):

$$\varepsilon = \beta\_hkl/(4 \operatorname{Tan} \Theta) \quad (5)$$

In addition, the lattice strain of the samples under consideration were calculated with the values 0.0049, 0.0131, 0.0101, 0.0024, and 0.0137 for $Cu_{0.1}FP$, $Cu_{0.5}FP$, $Cu_{1.0}FP$, $Cu_{0.5}F$, and Cu_0F nanocomposites, respectively. Introducing Cu^{2+} into the composition causes an increase in lattice strain with an increasing Cu^{+2} ratio. Moreover, the magnetic ions' inter-distances (sometimes referred to as hopping lengths) within the tetrahedral site $L_{A\text{-}A}$ (Å), the octahedral site $L_{B\text{-}B}$ (Å), and therefore the shared sites $L_{A\text{-}B}$ (Å) are calculated from XRD data using Eq. (6), Table 1.

$$L_{A\text{-}A} = \frac{a\sqrt{3}}{4}, \quad L_{B\text{-}B} = \frac{a\sqrt{2}}{4} \quad \text{and} \quad L_{A\text{-}B} = \frac{a\sqrt{11}}{4} \quad (6)$$

The values of hope length are also useful to determine the distance between the magnetic ions at A-site and B-sites (Sathisha et al., 2020).

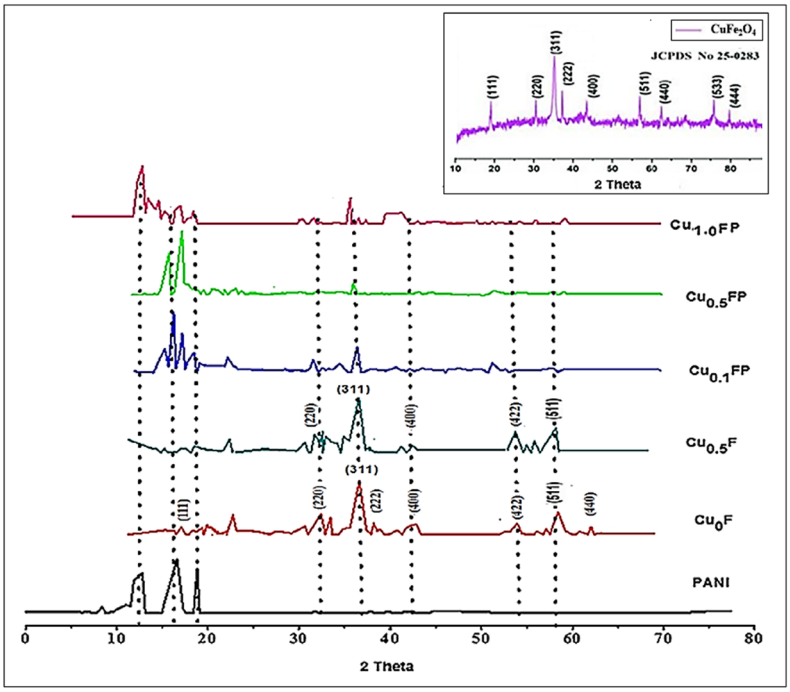

Fig. 1. Shows the XRD patterns of PANI, Cu_0F, $Cu_{0.5}F$, $Cu_{0.1}FP$, $Cu_{0.5}FP$, $Cu_{1.0}FP$, and $CuFe_2O_4$ nanocomposites (Science & Kumar, 2019)

TABLE 1. Presents the crystallite size (D), lattice constant (a), d spacing (Å), D_x, Lattice strain (ε), L_{A-A}, L_{B-B} (Å), and L_{A-B} of $Cu_{0.1}FP$, $Cu_{0.5}FP$, $Cu_{1.0}FP$, $Cu_{0.5}F$, and Cu_0F nanocomposites

Sample	Crystal size by XRD (nm)	Crystal size by TEM (nm)	Lattice constant (a) (Å)	d spacing (Å)	Dx (g/cm^3)	Lattice strain (ε)	L_{A-A} (Å)	L_{B-B} (Å)	L_{A-B} (Å)
$Cu_{0.1}FP$	11.95	8.218	7.469	2.252	-	0.0049	2.640	3.234	3.0965
$Cu_{0.5}FP$	10.95	-	8.590	2.59	-	0.0131	3.037	3.719	3.561
$Cu_{1.0}FP$	9.99	9.47	8.643	2.606	-	0.0101	3.055	3.7425	3.583
$Cu_{0.5}F$	6.82	3.37	8.357	2.52	5.4425	0.0024	2.954	3.61907	3.465
Cu_0F	1.50	-	8.301	2.503	5.5541	0.0137	2.935	3.5946	3.4416

FT-IR studies

FT-IR spectra of $CuFe_2O_4$ samples (Cu_0F and $Cu_{0.5}F$) show two absorption peaks at 418 and 561cm^{-1} assigned to the Fe-O and Cu-O bonds vibration modes on $CuFe_2O_4$, respectively (Fig. 2). This is consistent with the stretching vibration of octahedral sites and is associated with the peak at 418cm^{-1}, while that of tetrahedral sites is related to the peak at 561cm^{-1}. In addition, the broad peak at 3654 cm^{-1} reveals the surface stretching vibration of OH groups (Eivazzadeh-Keihan et al., 2021). After deposition of polyaniline, $Cu_xFe_{3-x}O_4$/PANI, the FT-IR spectra of PANI, $Cu_{0.1}FP$, $Cu_{0.5}FP$, and $Cu_{1.0}FP$ samples revealed the presence of new functional groups. As shown the bands observed at 1569, 1479, 1294, 1128, and 803cm^{-1} corresponding to the C=C stretching mode of the quinoid ring, the C-C stretching mode of the benzenoid ring, the C=N stretching mode of aromatic amine, the N=Q=N stretching of the quinoid rings, and the C-H out-plane bending of benzene rings, respectively (Neisi et al., 2019).

VSM studies

The magnetic properties of $Cu_{0.1}FP$, $Cu_{0.5}FP$, and $Cu_{1.0}FP$ nanocomposites were evaluated using the vibrating sample magnetometer technique (VSM), as seen in Fig. 3. Inspection of the hysteresis loops indicated that the magnetic fields in the nanocomposites are magnetically soft at ambient temperature and have a narrow shape. Moreover, the saturation magnetization (Ms) of the nanocomposites was reduced as the Cu^{+2} ratio increased with the values of 16emu/g, 11.5emu/g, and 8.7emu/g for x= 0.1, 0.5, and 1.0, respectively. Furthermore, increasing the Cu^{+2} ratios results in a thinner hysteresis curve.

SEM studies

Figure 4 shows the SEM micrographs of pristine PANI, $Cu_{0.1}F$, $Cu_{0.5}F$, $Cu_{0.1}FP$, $Cu_{0.5}FP$, and $Cu_{1.0}FP$ samples which revealed a small particle size, uniform morphology, and narrow size distribution. Moreover, the images of the $Cu_{0.1}F$ and $Cu_{0.5}F$ samples emphasized a particle collection with some residue, and the nanoparticles' grains are rigid and spherical. In addition, the spherical nature of the particles and the grain agglomeration were increased as the Cu^{+2} ratio was increased. Furthermore, the morphology of $CuFe_2O_4$ did not alter by PANI coating. Energy dispersive X-rays (EDX) were also utilized to analyze the elemental composition based on the samples' peak energy and weight percentages (Fig 5). The results revealed the existence of Cu, O, Fe, N, and C elements, which confirm the successful formation of $CuFe_2O_4$/PANI nanocomposites.

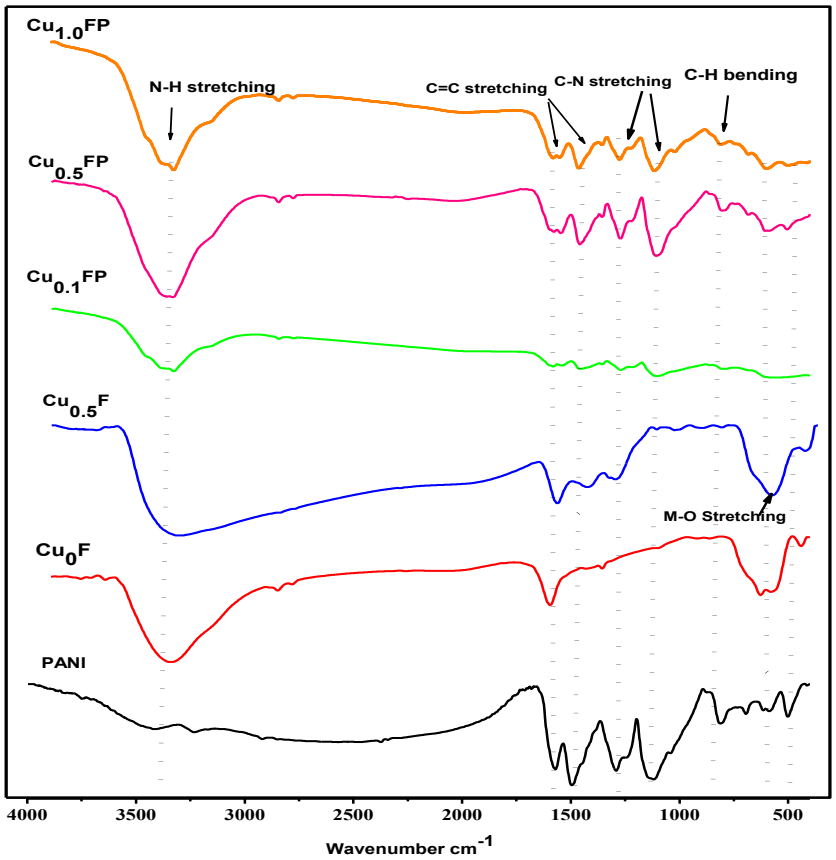

Fig. 2. FT-IR spectra of PANI, Cu_0F, $Cu_{0.5}F$, $Cu_{0.1}FP$, $Cu_{0.5}FP$, and $Cu_{1.0}FP$ nanocomposites

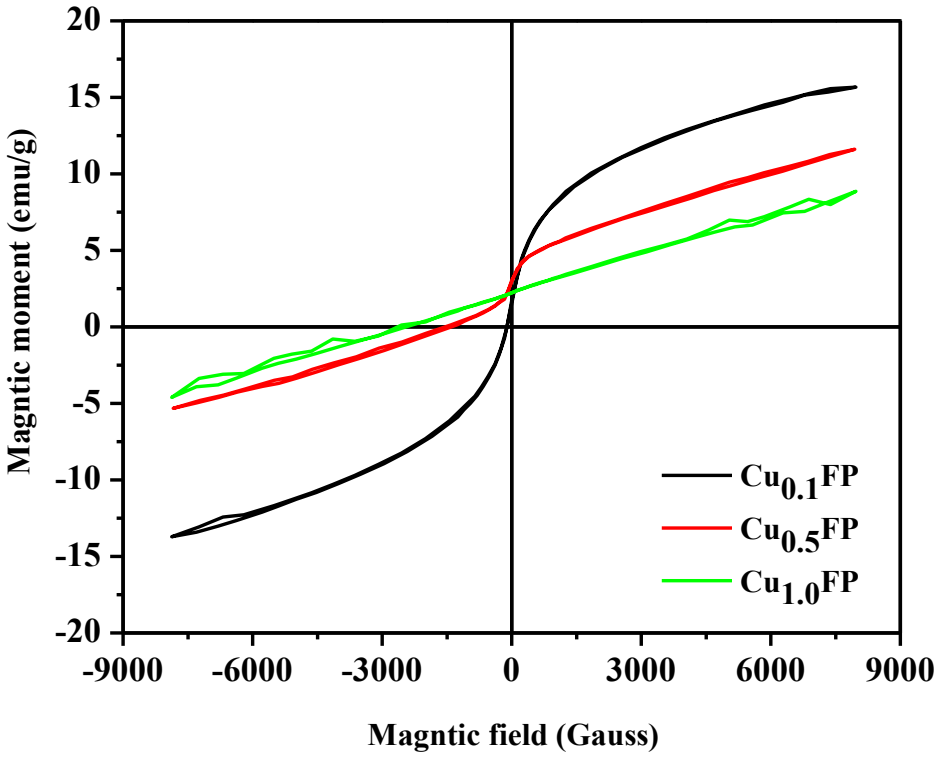

Fig. 3. Magnetic hysteresis loops of $Cu_{0.1}FP$, $Cu_{0.5}FP$, and $Cu_{1.0}FP$ nanocomposites at room temperature

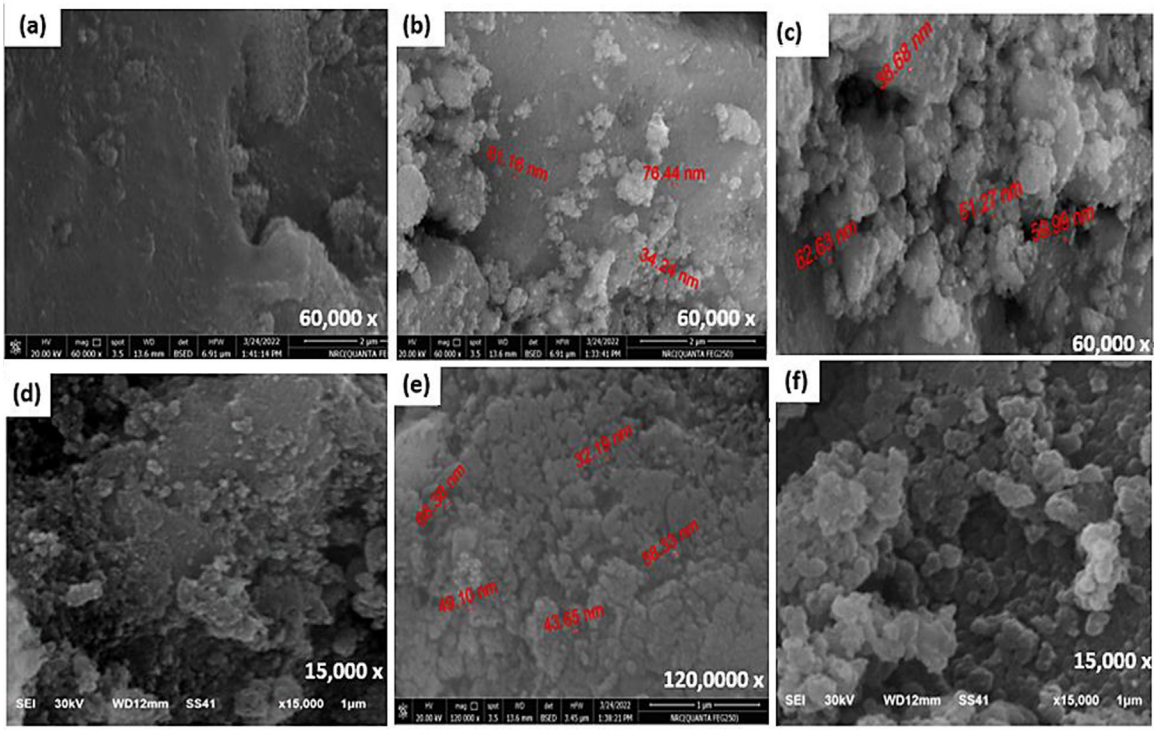

Fig. 4. High magnification scanning electron microscopy photographs of (a) Polyaniline, (b) $Cu_{0.1}F$, (c) $Cu_{0.5}F$, (d) $Cu_{0.1}FP$, (e) $Cu_{0.5}FP$, and (f) $Cu_{1.0}FP$ nanocomposites

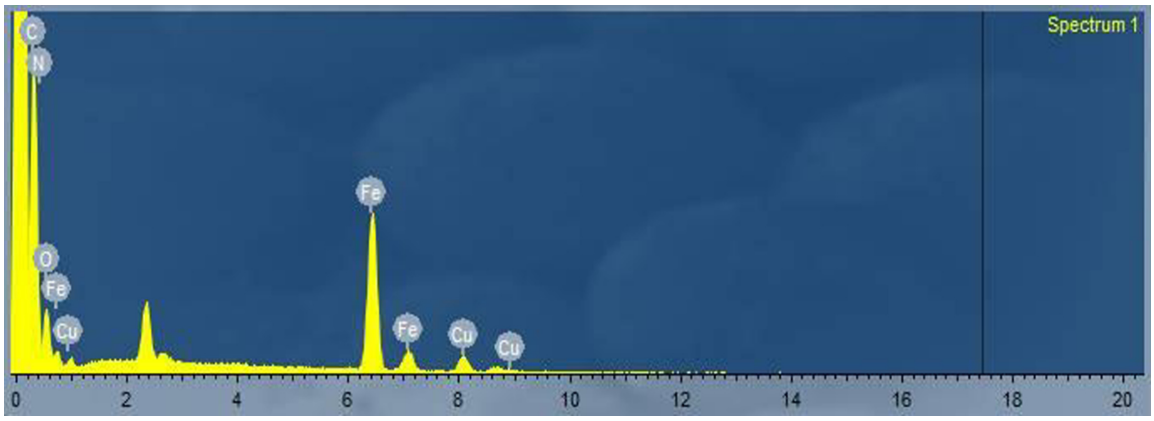

Fig. 5. EDX spectra $Cu_{1.0}FP$ nanocomposites

HR-TEM studies

Figure 6 (b-e) displays TEM images of $Cu_{0.5}F$, $Cu_{0.1}FP$, and $Cu_{1.0}FP$ nanocomposites which indicate the light shell character of PANI with a dark core of copper ferrite nanoparticles incorporated due to the differences in electron penetrability (Farghali et al., 2010). The produced ferrite nanoparticles have a crystalline spinal architecture of spherical and paralelloids with a particle size of 15–40nm. In addition, PANI wraps the ferrite nanoparticles and their aggregates, increasing the particle size of the nanocomposite up to 40nm, which verifies the interaction of ferrites with PANI without destroying the shape of the spherical particles and making the surface more cluttered and rough. The evenly brilliant concentric rings of the selected area electron diffraction (SAED) pattern show the sample powder's homogeneous distribution and polycrystalline nature. Moreover, the scattering pattern in the SAED image indicates the presence of crystals in a limited number of directions. Each concentric ring corresponds to a crystal plane with a specific "d" spacing, which can be measured to provide crystallographic information. Following the interplanar spacing, 0.76, 1.08, 1.16, 1.27, 1.52, and 1.26 Å were acquired from the SAED pattern

and recorded in Fig. 6f. The strong diffraction spots are designated using Miller indices with (220), (311), (222), (400), (511), and (440), indicating that the $CuFe_2O_4$ nanoparticles show crystalline nature with clear circular spots (George & Abraham, 2021).

XPS measurements

The X-ray photoelectron spectra studies were performed to reveal the compositional characterization of the $CuFe_2O_4$/PANI nano ferrite sample. Figure 7 reveals that several signals are coexistent. Numerous chemical species were investigated based on their positions and binding types. According to the XPS survey spectrum, chemical species were determined depending on their positions, binding types, and element content. According to the XPS survey spectrum, Fig. 7 (a) indicates that the primary constituent elements were C, O, Fe, N, Cu, and S at different binding energies. The percentage of chemical composition of $CuFe_2O_4$/PANI by XPS spectrum is C 1s (56.36%), O 1s (26.40%), Fe 2p (5.77%), N 1s (7.90%), Cu 2p3 (1.05%) and S 2p (2.52%). As shown in Fig. 7 (b), the peak at 956.04 eV in the Cu 2p XPS spectrum is associated with the Cu (I) species. The peak at 935.36 eV is assigned to 2p3/2 of Cu^{+2} (Fan et al., 2009; Wang et al., 2020). The peak is situated at 956.03 eV, and its shakeup satellite at 961.60 eV relates to Cu 2p1/2 (Yao et al., 2015). In the Fe 2p XPS spectrum shown in Fig. 7 (c), six distinct peaks are located at 711.11eV, 714.17eV, 718.02 eV, 724.97eV, 728.27eV, and 733.18eV, respectively. The highest peak, at 711.11 eV, can be attributed to the 2p3/2 of Fe^{3+} (Qian et al., 2017). The peaks at 714.17eV and 724.97 eV are related to the binding energies of 2p3/2 and 2p1/2 for Fe^{2+} (Peng et al., 2013). The peak appearing at 728.27 eV is attributed to the 2p1/2 of Fe^{3+} and Fe^{2+}, and the peak observed at 718.02eV can be considered as a satellite for the four peaks mentioned above, demonstrating the good coexistence of Fe^{3+} and Fe^{2+} in the PANI/$CuFe_2O_4$ nanocomposite (Su et al., 2014). For the O 1s XPS spectrum in Fig. 7 (d), three peaks with a binding energy of 532.33 eV, 531.31 eV, and 529.9eV are contributed by the lattice oxide-oxygen of Fe-O and Cu-O (Li et al., 2019). The N 1s XPS spectrum in Fig. 7 (e) shows two main peaks at 399.44eV and 399.51eV, assigned to the NH^{2+}- and -N= groups, respectively. Peaks at 401.73eV are due to the amine group (-NH-) and cationic species (=NH^+-), respectively, indicating that the aniline was successfully polymerized (Salvatierra et al., 2015; Zhang et al., 2020). The C 1s XPS spectrum in Fig. 7(f) shows a dominant peak at 284.44 eV caused by C=C (sp^2-carbon), followed by two lower peaks at 287.32eV and 285.92eV caused by sp3-hybridized carbon. The sulfur content could be attributed to adsorbed SO_4^{-2} anions as counter ions on polyaniline chains.

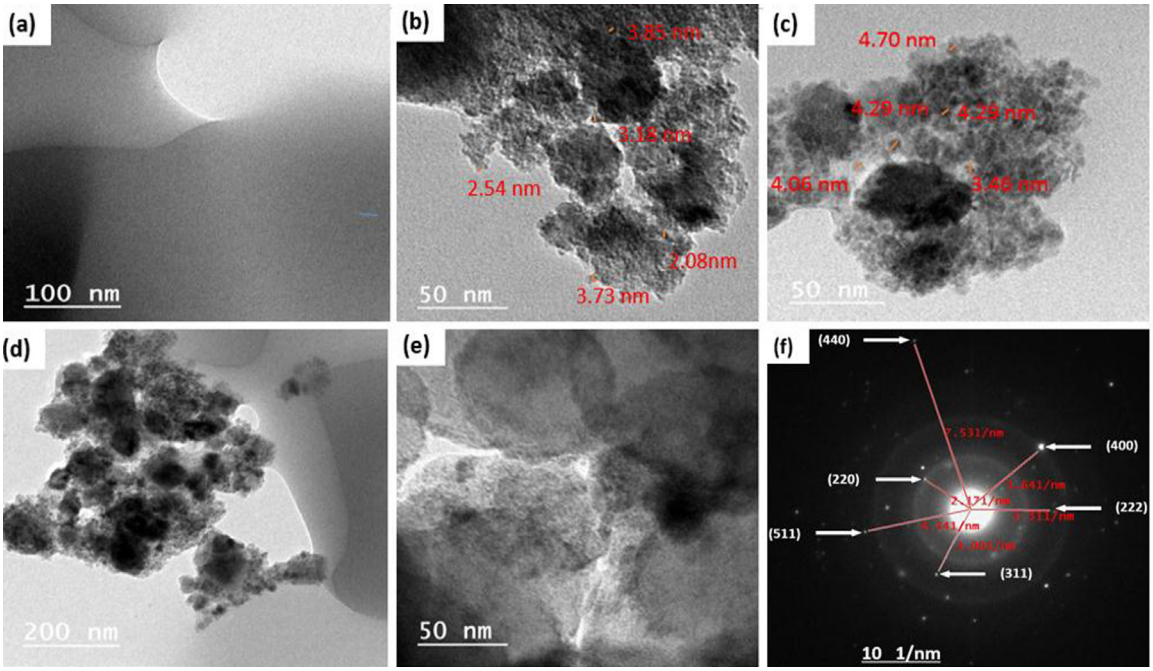

Fig. 6. HRTEM photographs of (a) PANI, (b) $Cu_{0.5}F$, (c, d) $Cu_{0.1}FP$, (e) $Cu_{1.0}FP$, and (f) SAED of $Cu_{1.0}FP$ nanocomposites

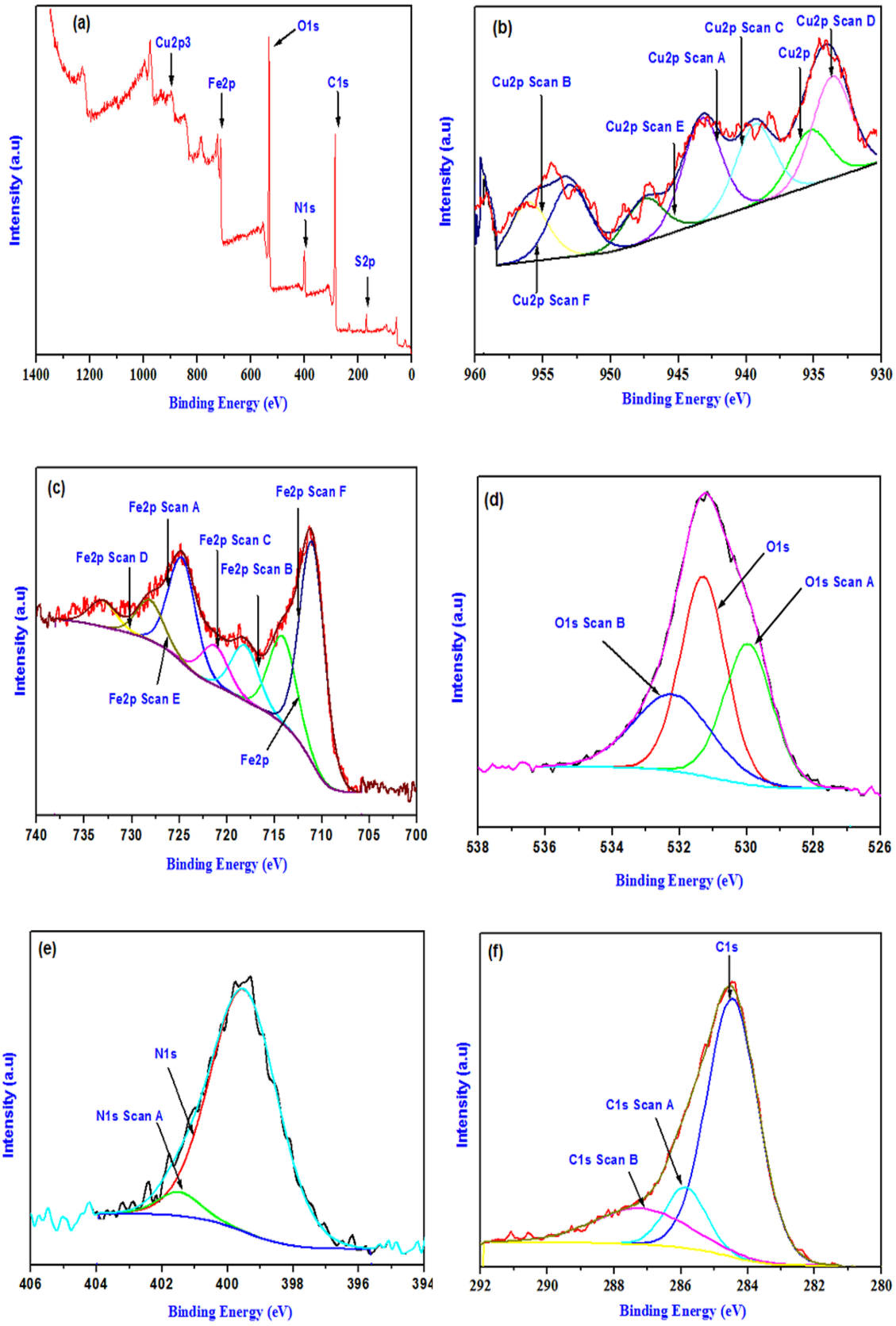

Fig.7. XPS spectra $Cu_{1.0}FP$ nanocomposites

Evaluation of antimicrobial properties

The results showed that the negative control (DMSO) did not influence bacterial growth. In contrast, the positive control had a maximum zone of inhibition compared with $Cu_xFe_{3-x}O_4$NPs and $Cu_xFe_{3-x}O_4$/PANI (10 x 10^{-4} mg/mL of NPS). Figure 8 demonstrates the antimicrobial activity of $Cu_xFe_{3-x}O_4$ nanoparticles and $Cu_xFe_{3-x}O_4$/PANI nanocomposites against Gram-positive (*Staph*), Gram-negative (*E. coli, P. aeruginosa*, and *K. pneumoniae*), and Fungi such as (*C. albicans*). Clearly, the antimicrobial efficiency was increased with increasing of Cu^{2+} ratio with the order; $Cu_{1.0}Fe_2O_4 > Cu_{0.5}Fe_{2.5}O_4 > Cu_{0.1}Fe_{2.9}O_4 > Cu_0Fe_3O_4$ NPs (Fig. 9). The same results have been observed in the case of $Cu_xFe_{3-x}O_4$/PANI nanocomposites with the order; $Cu_{1.0}Fe_2O_4$/PANI > $Cu_{0.5}Fe_{2.5}O_4$ / PANI > $Cu_{0.1}Fe_{2.9}O_4$/PANI nanocomposites as shown in Table 2 and Fig. 10.

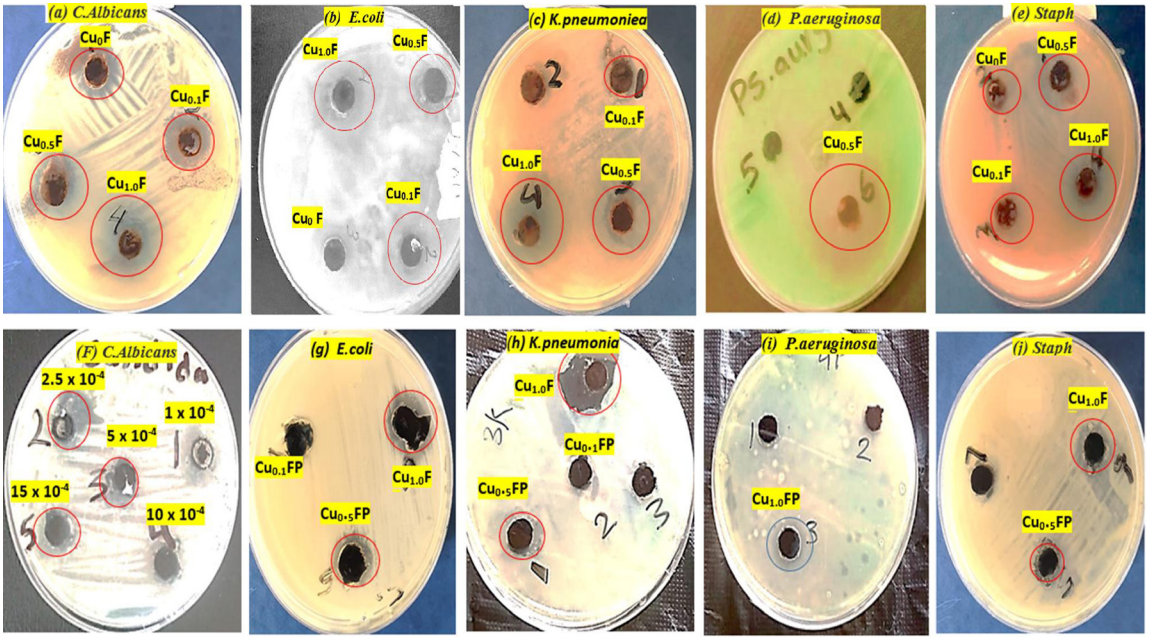

Fig. 8. Zone of inhibition (ZOI) graph of $Cu_xFe_{3-x}O_4$ nanoparticles (a-d), against (a) *C. albicans*, (b) *E. coli*, (c) *K. pneumonia*, (d) *P. aeruginosa*, (e) *Staph aureus,* and $CuFe_2O_4$/PANI nanocomposites. (f-j) against, (f) *C. albicans,* (g) *E. coli,* (h) *K. pneumonia*, (i) *P. aeruginos*a, and (j) *Staph. aureus*

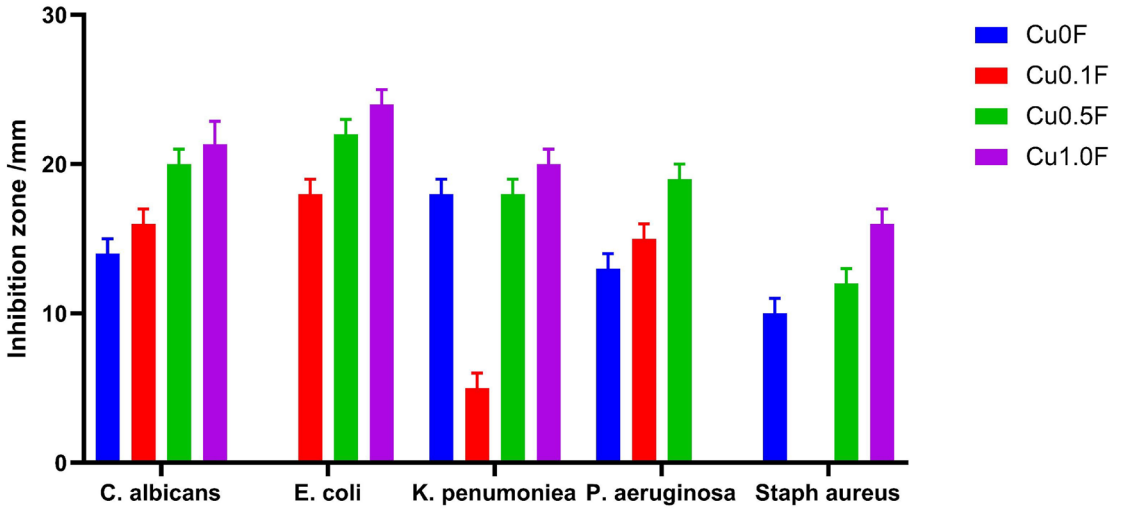

Fig. 9. $Cu_xFe_{3-x}O_4$ nanoparticle inhibition zone against *C. albicans*, *E. coli*, *K. pneumoniae*, *P. aeruginosa*, and *Staph. aureus*

TABLE 2. Antibacterial and antifungal properties of $Cu_xFe_{3-x}O_4$ nanoparticle and $Cu_xFe_{3-x}O_4$/PANI nanocomposites

Micro-organism	Inhibition zone (mm)				Inhibition zone (mm)		
	Cu_0F	$Cu_{0.1}F$	$Cu_{0.5}F$	$Cu_{1.0}F$	$Cu_{0.1}FP$	$Cu_{0.5}FP$	$Cu_{1.0}FP$
C. albicans	15	16	20	21	8	14	19.0
E. coli	0	18	22	24	0	16	17.9
K. penumoniea	17	5	18	20	0	18	22.0
P. aeruginosa	12	15	19	0	0	0	18.0
Staph	9	0	12	16	0	12	15.0

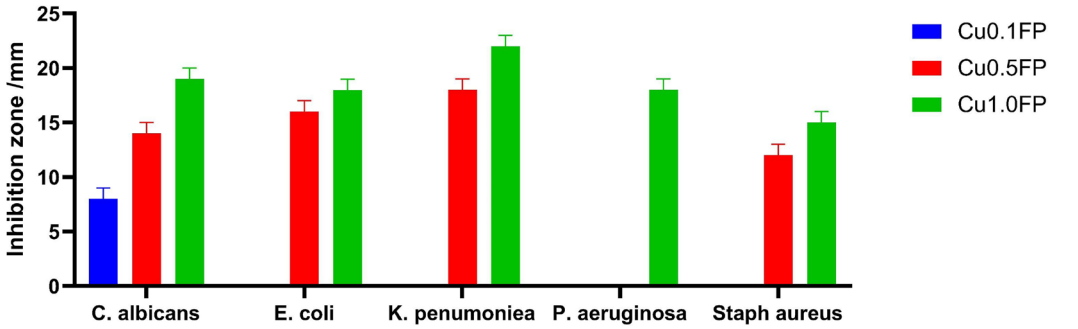

Fig. 10. The inhibition zone of $Cu_xFe_{3-x}O_4$/PANI nanocomposites against *C. albicans*, *E. coli*, *K. pneumoniea*, and *Staph. aureus*

Determination of the minimum inhibitory concentration

The minimum inhibitory concentration (MIC) values of the $Cu_xFe_{3-x}O_4$ nanoparticles and $Cu_xFe_{3-x}O_4$/PANI nanocomposite were determined at different concentrations; 1 x 10^{-4}, 2.5 x 10^{-4}, 5 x 10^{-4}, 10 x 10^{-4}, and 15 x 10^{-4}mg/mL. The MICs values of $Cu_{0.5}F$ NPs were recorded at 10 x 10^{-4}mg/mL for *C. albicans* and *K. pneumonia* and 2.5 x 10^{-4}mg/mL for *E. coli* (Fig. 11, Table 3). The maximum concentration of $Cu_{0.5}F$ NPs was recorded at 15 x 10^{-4}mg/mL for *C. albicans, E. coli,* and *K. pneumonia* and displayed high bioactivity and completely inhibited colony growth. The MIC values of $Cu_{0.5}FP$, and Cu_1FP nanocomposite against *C. albicans*, *E. coli, K. pneumoniea, P. aeruginosa,* and *Staph* were 10 x 10^{-4}mg/mL (Figs. 12, 13 and Table 3).

SEM examination of K. pneumoniae and C. albicans Biofilms

The morphologies of *C. albicans* and *K. pneumoniae* cells were investigated by SEM. In negative untreated controls, cells are smoother and keep their respective morphologies. As shown in Fig. 14 (a, c), *C. albicans* revealed a round shape while *K. pneumoniae* showed a rod-like shape. In contrast, the microbial cells exposed to $Cu_{0.5}FP$ nanocomposite showed surface roughness and shape changes, Fig. 14 (b, d). Several holes on the membrane's surface of *C. albicans* were also observed.

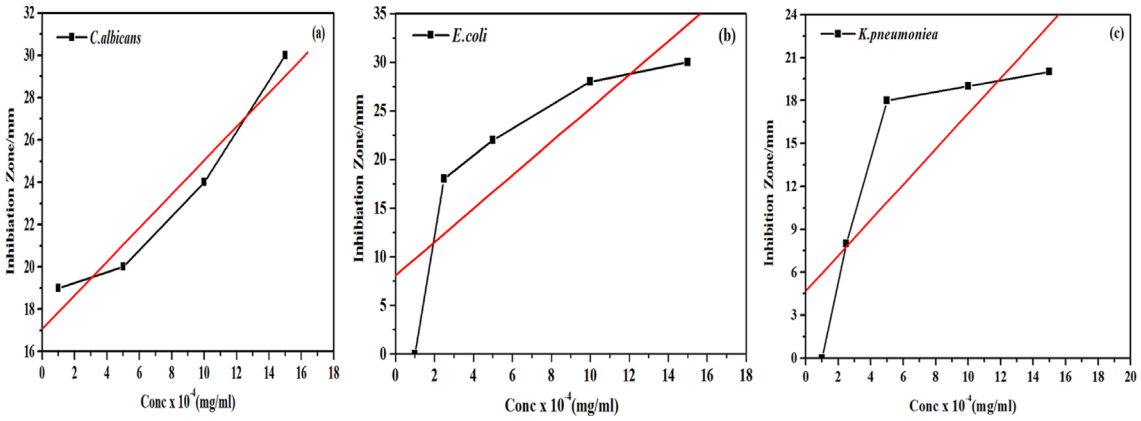

Fig. 11. MIC values of $Cu_{0.5}F$ NPs in mg/mL against (a) *C. albicans,* (b) *E. coli*, and (c) *K. pneumonia*

TABLE 3. displays the average inhibition zones obtained from various nanocomposites containing $Cu_{0.5}F$ nanoparticles and $Cu_{0.5}FP$, $Cu_{1.0}FP$ nanocomposites against a variety of microbes

Micro-organism	MIC values in mg/mL ($Cu_{0.5}F$) x 10^{-4}					MIC values in mg/mL ($Cu_{0.5}FP$) x 10^{-4}				MIC values in mg/mL ($Cu_{1.0}FP$) x 10^{-4}				
	1	2.5	5	10	15	1	2.5	5	10	1	2.5	5	10	15
C. albicans	19	-	20	24	30	13	14	17	16	0	18	19	0	18
E. coli	0	18	22	28	30	-	-	-	-	-	-	-	-	
K. penumoniea	0	8	18	19	22	16	18	19	22	9	18	20	21	22
P. aeruginosa	-	-		-	-	-	-	-	-	11	12	18	19	20
Staph.	-	-		-	-	-	-	-	-	8	12	15	20	19.5

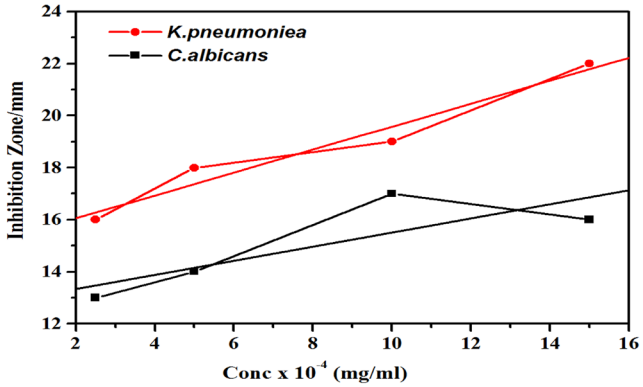

Fig. 12. Shows the MIC values of $Cu_{0.5}FP$ nanocomposites in mg/mL

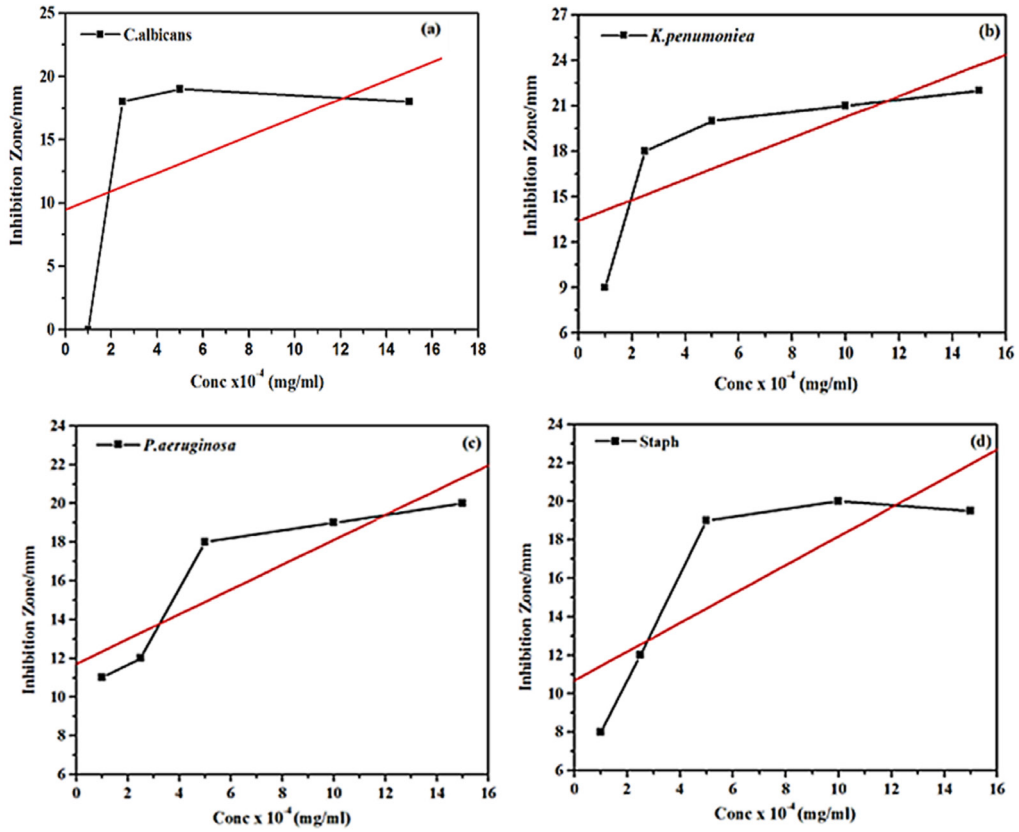

Fig. 13. MIC values of $Cu_{1.0}FP$ nanocomposites against (a) *C. albicans*, (b) *K. pneumoniea*, (c) *P. aeruginosa*, and (d) *Staph. aureus*

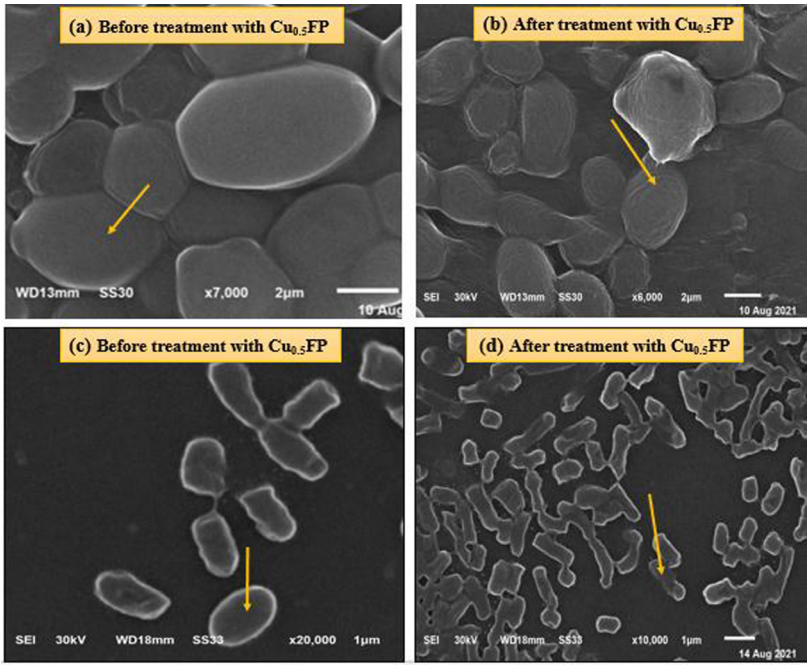

Fig. 14. SEM images of (a, b) *C. albicans* and (c, d) *K. pneumonia* before and after treatment with $Cu_{0.5}FP$ nanocomposites

Discussion

In general, the mechanism of the antibacterial activity of ferrite nanoparticles can be described by the release of dissociated metal ions and reactive oxygen species (ROS). Several factors such as the crystal size of nanoparticles or nanocomposites, the Cu^{2+} content in the specimen, and combining copper ferrite nanoparticles with PANI are all significant aspects to be responsible. This study verified and improved the $Cu_xFe_{3-x}O_4$/PANI nanocomposite's broad-spectrum antibacterial activity by demonstrating that they can suppress the multiplication of wild-type and medically important antibiotic-resistant gram-negative and gram-positive pathogens. The combinations of $Cu_xFe_{3-x}O_4$ nanoparticles and $Cu_xFe_{3-x}O_4$/PANI nanocomposite were described and tested for antibacterial activity against *Staphylococcus aureus, E. coli, Pseudomonas aeruginosa, Klebsiella pneumoniae, and Candida albicans*. The results showed that the $Cu_xFe_{3-x}O_4$NPS and $Cu_xFe_{3-x}O_4$/PANI nanocomposites exposed higher antibacterial activity against gram-negative bacteria and Candida albicans than gram-positive bacteria. Increasing the Cu^{+2} ratios led to increase in the antimicrobial activity due to the decrease in crystalline size, which provides better penetration of the microorganisms' cell walls. Several studies reported that the antibacterial activity of metallic nanoparticles was based on their shape and size (Prodan et al., 2013a; Gomes et al., 2018). Moreover, the result showed clear growth inhibitory effects against gram-negative bacteria and candida rather than gram-positive bacteria in the following order: K. *pneumoniae* > *Staph* for $Cu_{0.1}F$ NPs and *E. coli* > *C. albicans* > *P. aeruginosa* > *K. pneumoniae* > *Staph* for $Cu_{0.5}F$ NPs, and *K. pneumoniae* > *C. albicans* > *P. aeruginosa* > *E. coli* > *Staph* for $Cu_{1.0}FP$ nanocomposites. In addition, the antibacterial properties of PANI constituent could be explained by electrostatic adhesion between the polymer backbone and bacteria, which carries charges of different signs, causing the bacteria's walls to break down and intracellular fluid to flow out, resulting in death (Shai, 2002; Strahl & Hamoen, 2010; Gizdavic-Nikolaidis et al., 2011). Furthermore, copper ions may bind to DNA molecules disrupting their helical causing failure of the biochemical activities in bacterial cells (Abboud et al., 2014). Due to the success of copper ions, the nanoparticles attach to the bacterial wall and penetrate through the cell membrane, promoting the disintegration and disappearance of cytoplasm and the destruction of the bacterium's cell wall, leading the cell to death (Scheme 2) (Gomes et al., 2018). Moreover, Cu^{2+} ions can disrupt the bacterial envelope by increasing cytoplasmic membrane permeability via ions interacting with sulfur and phosphorus in DNA, causing DNA replication, cell reproduction,

and even microorganism death problems. Denaturation of cytoplasmic ribosomes by copper ions can also inhibit protein synthesis (Yin et al., 2020). Also, $Cu_xFe_{3-x}O_4$ NPs and $Cu_xFe_{3-x}O_4$/PANI nanocomposite demonstrated antifungal behavior. The death of *C. albicans* could be ascribed to the loss of fungal membrane integrity and the ability of Cu^{+2} to penetrate the cytoplasm of *C. albicans* leading to cell wall alterations (Mart et al., 2020). The obtained results might be due to the active oxygen species released from ferrites, which can penetrate the cell wall and enhance antimicrobial activity, leading to death (Gheidari et al., 2020). These results showed that prepared $Cu_xFe_{3-x}O_4$ NPs and $Cu_xFe_{3-x}O_4$/PANI nanocomposites were more effective against gram-negative bacteria and *C. albicans* than gram-positive bacteria. Furthermore, $Cu_xFe_{3-x}O_4$ NPs showed significantly higher antimicrobial activity than $Cu_xFe_{3-x}O_4$/PANI.

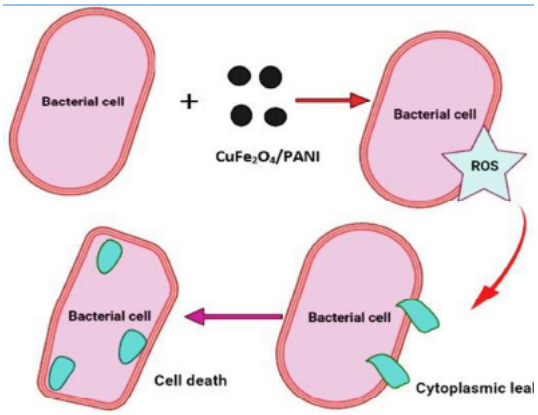

Scheme 2. Schematic of the antibacterial mechanism of the $CuFe_2O_4$/PANI nanocomposites

Conclusion

Copper ferrites with various Cu^{2+} rations and their nanocomposites, and after combining with PANI, were successfully prepared and characterized by different sophisticated techniques. The nanoparticles demonstrated three important properties that must be verified in antimicrobial agents: Crystallite size at the nanoscale, the sufficient amount of copper ions, and superparamagnetic behavior. The materials were combined with PANI via a simple oxidative polymerization reaction. In practice, the materials exhibited improved antimicrobial activity characterized by an increasing the Cu^{2+} ratio, a decrease in the crystallite size, and after doping with PANI. These non-toxic, simple-to-prepare, and inexpensive antibacterial materials can be widely used in various fields, such as packaging materials and preservatives.

Funding: There was no funding for this study. The authors paid for all experiments and data analysis.

Conflict of interest: The authors conclude that they have no conflicts of interest.

Author contributions: Mohammed A. Eid; carried out the experimental antimicrobial work and the critical review and wrote the draft manuscript. *Abeer A. El-Helaly*; carried out the experimental work and wrote the draft manuscript. *Ali H. Gemeay;* a critical thinking, expert opinion, and supervision *Mohamed Y. El-Sheikh and Hosny A. El-Daly;* Conceptualization and supervision of the manuscript. All authors contributed to the study article and approved the final version.

References

Abboud, Y., Saffaj, T., Chagraoui, A., El Bouari, A., Brouzi, K., Tanane, O., Ihssane, B. (2014) Biosynthesis, characterization and antimicrobial activity of copper oxide nanoparticles (CONPs) produced using brown alga extract (Bifurcaria bifurcata), *Applied Nanoscience (Switzerland)*, **4**(5), 571–576.

Ali, S.Y., Eid, O.I., Siddig, M.A. (2020) The Influence of Cu on the Dielectric Properties of $NiZnFe_2O_4$ Synthesized by Solid State Reaction Method, *Journal of Materials Science and Chemical Engineering*, **08**(09), 14–23.

Altincekic, T.G., Boz, İ.S.M.A.İ.L., Baykal, A., Kazan, S., Topkaya, R., Toprak, M.S. (2010) Synthesis and characterization of $CuFe_2O_4$ nanorods synthesized by polyol route. *Journal of Alloys and Compounds*, **493**(1–2), 493–498.

Amiri, M., Eskandari, K., Salavati-Niasari, M. (2019a) Magnetically retrievable ferrite nanoparticles in the catalysis application, *Advances in Colloid and Interface Science*, **271**, 101982. doi: 10.1016/j.cis.2019.07.003.

Amiri, M., Salavati-Niasari, M., Akbari, A. (2019b) Magnetic nanocarriers: Evolution of spinel ferrites for medical applications, *Advances in Colloid and Interface Science*, **265**, 29–44.

Arakha, M., Pal, S., Samantarrai, D., Panigrahi, T. K., Mallick, B.C., Pramanik, K., Mallick, B., Jha,

S. (2015) Antimicrobial activity of iron oxide nanoparticle upon modulation of nanoparticle-bacteria interface. *Scientific Reports,* **5**, 1–12.

Araújo, J.F.D.F., Pereira, J.M.B., Bruno, A.C. (2019) Assembling a magnetometer for measuring the magnetic properties of iron oxide microparticles in the classroom laboratory. *American Journal of Physics*, **87**(6), 471–475.

Assar, S.T., Abosheiasha, H.F., Saafan, S.A., El Nimr, M.K. (2015) Preparation, characterization and magnetization of nano and bulk $Ni_{0.5}Co_{0.5-2x}Li_xFe_{2+x}O_4$ samples. *Journal of Molecular Structure*, **1084**, 128–134.

Ates, M. (2011) Review study of electrochemical impedance spectroscopy and equivalent electrical circuits of conducting polymers on carbon surfaces. *Progress in Organic Coatings*, **71**(1), 1–10. https://doi.org/10.1016/j.porgcoat.2010.12.011.

Chudobova, D., Cihalova, K., Kopel, P., Melichar, L., Ruttkay-nedecky, B., Vaculovicova, M., Adam, V., Kizek, R. (2015) Complexes of Metal-Based Nanoparticles with Chitosan Suppressing the Risk of *Staphylococcus aureus* and *Escherichia coli* Infections. *Nanotechnology in Diagnosis, Treatment and Prophylaxis of Infectious Diseases*. Elsevier Inc. https://doi.org/10.1016/B978-0-12-801317-5.00013-X.

Dhiman, R.L., Taneja, S.P., Reddy, V.R. (2008) Preparation and Characterization of Manganese Ferrite Aluminates. *Advances in Condensed Matter Physics*, **2008**, 1–7. https://doi.org/10.1155/2008/703479.

Eivazzadeh-Keihan, R., Asgharnasl, S., Bani, M. S., Radinekiyan, F., Maleki, A., Mahdavi, M., Babaniamansour, P., Bahreinizad, H., Shalan, A. E., Lanceros-Méndez, S. (2021) Magnetic Copper Ferrite Nanoparticles Functionalized by Aromatic Polyamide Chains for Hyperthermia Applications. *Langmuir*, **37**(29), 8847–8854.

Fan, J., Dai, Y., Li, Y., Zheng, N., Guo, J., Yan, X., Stucky, G.D. (2009) Low-temperature, highly selective, gas-phase oxidation of benzyl alcohol over mesoporous K-Cu-TiO_2 with stable copper(I) oxidation state. *Journal of the American Chemical Society*, **131**(43), 15568–15569.

Farghali, A.A., Moussa, M., Khedr, M.H. (2010) Synthesis and characterization of novel conductive and magnetic nano-composites. *Journal of Alloys and Compounds*, **499**(1), 98–103.

Gemeay, A.H., Keshta, B.E., El-Sharkawy, R.G., Zaki, A.B. (2020) Chemical insight into the adsorption of reactive wool dyes onto amine-functionalized magnetite/silica core-shell from industrial wastewaters. *Environmental Science and Pollution Research*, **27**(26), 32341–32358.

George, J., Abraham, K.E. (2021) The structural phase change of copper ferrite and its gas-sensing properties. *Journal of Materials Science: Materials in Electronics*, **32**(10), 13220–13238.

Ghaani, M., Saffari, J. (2016) Synthesis of $CuFe_2O_4$ Nanoparticles by a new co-precipitation method and using them as Efficient Catalyst for One-pot Synthesis of Naphthoxazinones. *Journal of Nanostructures*, **6**(2), 172–178.

Gheidari, D., Mehrdad, M., Maleki, S., Hosseini, S. (2020) Synthesis and potent antimicrobial activity of $CoFe_2O_4$ nanoparticles under visible light. *Heliyon*, **6**(10), e05058. https://doi.org/10.1016/j.heliyon.2020.e05058.

Gizdavic-Nikolaidis, M.R., Bennett, J.R., Swift, S., Easteal, A.J., Ambrose, M. (2011) Broad spectrum antimicrobial activity of functionalized polyanilines. *Acta Biomaterialia*, **7**(12), 4204–4209.

Gomes, G.A., Da Costa, G.L., Da Silva Figueiredo, A.B.H. (2018) Synthesis of ferrite nanoparticles $Cu_{1-x}Ag_xFe_2O_4$ and evaluation of potential antibacterial activity. *Journal of Materials Research and Technology*, **7**(3), 381–386.

Goya, G.F., Rechenberg, H.R., Jiang, J.Z. (1998) Structural and magnetic properties of ball milled copper ferrite. *Journal of Applied Physics*, **84**(2), 1101–1108.

Hegazy, E.Z., Abd El-Maksod, I.H., Ibrahim, A.M., El-Shafay, S.E.-S. (2018) New insights about the formation of copper ferrite: in situ X-ray diffraction study. *Bulletin of the National Research Centre*, **42**(1), 0–4. https://doi.org/10.1186/s42269-018-0010-9.

Kefeni, K.K., Mamba, B.B., Msagati, T.A.M. (2017) Application of spinel ferrite nanoparticles in water

and wastewater treatment: A review. *Separation and Purification Technology*, **188**, 399–422.

Kharazi, P., Rahimi, R., Rabbani, M. (2019) Copper ferrite-polyaniline nanocomposite: Structural, thermal, magnetic and dye adsorption properties. *Solid State Sciences*, **93**, 95–100.

Kurian, J., Lahiri, B.B., Mathew, M.J., Philip, J. (2021) High magnetic fluid hyperthermia efficiency in copper ferrite nanoparticles prepared by solvothermal and hydrothermal methods. *Journal of Magnetism and Magnetic Materials*, **538**(August 2020), 168233. https://doi.org/10.1016/j.jmmm.2021.168233.

Li, R., Cai, M., Xie, Z., Zhang, Q., Zeng, Y., Liu, H., Liu, G., Lv, W. (2019) Construction of heterostructured $CuFe_2O_4$/g-C_3N_4 nanocomposite as an efficient visible light photocatalyst with peroxydisulfate for the organic oxidation. *Applied Catalysis B: Environmental*, **244**, 974–982.

Liu, B.L., Eu, Y.P., Wang, M.L. (2009) Magnetic and catalytic properties of copper ferrite nanopowders prepared by combustion process. *Journal of Nanoscience and Nanotechnology*, **9**(2), 1491–1495.

Liu, F., Yuan, Y., Li, L., Shang, S., Yu, X., Zhang, Q., Jiang, S., Wu, Y. (2015) Synthesis of polypyrrole nanocomposites decorated with silver nanoparticles with electrocatalysis and antibacterial property. *Composites Part B: Engineering*, **69**, 232–236.

Manova, E., Tsoncheva, T., Paneva, D., Popova, M., Velinov, N., Kunev, B., Tenchev, K., Mitov, I. (2011) Nanosized copper ferrite materials: Mechanochemical synthesis and characterization. *Journal of Solid State Chemistry*, **184**(5), 1153–1158.

Martínez, A., Apip, C., Meléndrez, M. F., Domínguez, M., Sánchez-Sanhueza, G., Marzialetti, T., Catalán, A. (2021) Dual antifungal activity against *Candida albicans* of copper metallic nanostructures and hierarchical copper oxide marigold-like nanostructures grown in situ in the culture medium. *Journal of Applied Microbiology*, **130**(6), 1883-1892.

Masunga, N., Mmelesi, O.K., Kefeni, K.K., Mamba, B.B. (2019) Recent advances in copper ferrite nanoparticles and nanocomposites synthesis, magnetic properties and application in water treatment: Review. *Journal of Environmental Chemical Engineering*, **7**(3), 103179.

Mulud, F.H., Dahham, N.A., Waheed, I.F. (2020) Synthesis and Characterization of Copper Ferrite Nanoparticles. *IOP Conference Series: Materials Science and Engineering*, **928**(7), 0–11.

Neisi, Z., Ansari-Asl, Z., Dezfuli, A.S. (2019) Polyaniline/Cu(II) metal-organic frameworks composite for high performance supercapacitor electrode. *Journal of Inorganic and Organometallic Polymers and Materials*, **29**(6), 1838–1847.

Peng, H., Mo, Z., Liao, S., Liang, H., Yang, L., Luo, F., Song, H., Zhong, Y., Zhang, B. (2013) High performance Fe- and N- Doped carbon catalyst with graphene structure for oxygen reduction. *Scientific Reports*, **3**, 1–7. https://doi.org/10.1038/srep01765.

Pham, T., Lee, B. (2014) Applied Surface Science Cu doped TiO_2 / GF for photocatalytic disinfection of Escherichia coli in bioaerosols under visible light irradiation : Application and mechanism. *Applied Surface Science*, **296**, 15–23.

Predoi, D., Iconaru, S.L., Predoi, M.V., Buton, N., Megier, C., Motelica-Heino, M. (2019) Biocompatible layers obtained from functionalized iron oxide nanoparticles in suspension. *Coatings*, **9**(12). https://doi.org/10.3390/coatings9120773.

Predoi, D., Iconaru, S.L., Predoi, M.V., Motelica-Heino, M. (2020) Removal and oxidation of as(III) from water using iron oxide coated CTAB as adsorbent. *Polymers*, **12**(8). https://doi.org/10.3390/POLYM12081687.

Prodan, A.M., Iconaru, S.L., Chifiriuc, C.M., Bleotu, C., Ciobanu, C.S., Motelica-Heino, M., Sizaret, S., Predoi, D. (2013a) Magnetic properties and biological activity evaluation of iron oxide nanoparticles. *Journal of Nanomaterials*, **2013**. https://doi.org/10.1155/2013/893970.

Prodan, A.M., Iconaru, S.L., Ciobanu, C.S., Chifiriuc, M.C., Stoicea, M., Predoi, D. (2013b) Iron oxide magnetic nanoparticles : Characterization and toxicity evaluation by *in vitro* and *in vivo* Assays, *Journal of Nanomaterials*, **2013**. doi: 10.1155/2013/587021.

Qian, X., Ren, M., Zhu, Y., Yue, D., Han, Y., Jia, J.,

Zhao, Y. (2017) Visible light assisted heterogeneous Fenton-like degradation of organic pollutant via α-FeOOH/mesoporous carbon composites. *Environmental Science and Technology*, **51**(7), 3993–4000.

Qindeel, R., Alonizan, N.H., Alghamdi, E.A., Awad, M.A. (2021) Synthesis and characterization of spinel ferrites for microwave devices. *Journal of Sol-Gel Science and Technology*, **97**(3), 593–599.

Rajput, J.K., Arora, P., Kaur, G., Kaur, M. (2015) $CuFe_2O_4$ magnetic heterogeneous nanocatalyst: Low power sonochemical-coprecipitation preparation and applications in synthesis of 4H-chromene-3-carbonitrile scaffolds. *Ultrasonics Sonochemistry*, **26**, 229–240.

Rashad, M.M., Soltan, S., Ramadan, A.A., Bekheet, M.F., Rayan, D.A. (2015) Investigation of the structural, optical and magnetic properties of CuO/ $CuFe_2O_4$ nanocomposites synthesized via simple microemulsion method. *Ceramics International*, **41**(9), 12237–12245.

Rather, S., Saeed, U., Al-zahrani, A.A., Bamufleh, H.S., Alhumade, H.A., Taimoor, A.A., Lemine, O.M., Ali, A.M., Zaitone, B., Al, Alam, M.M. (2021) Doped Nanostructured Manganese Ferrites : Synthesis, Characterization, and Magnetic Properties. *Journal of Nanomaterials,* **2021**. Article ID 9410074 | https://doi.org/10.1155/2021/9410074

Saafan, S., Elghazzawy, E., Abo-Aita, N. (2021) Preparation and structural investigation of Polyethylene glycol (PEG)/ nano-ferrite composites. *Egyptian Journal of Solids*, **43**(1), 174–191.

Ramiza, F.A., Ajmal, S.K., Khan, M.B., Nasim, A., Jamil, Y., Kashif, K., Amira, S. (2016) Effect of UV radiations to control particle size of Mn-Zn spinel ferrite nanoparticles, In: *IOP Conference Series: Materials Science and Engineering*, **146**(1). doi: 10.1088/1757-899X/146/1/012029.

Salavati-Niasari, M., Mahmoudi, T., Sabet, M., Hosseinpour-Mashkani, S.M., Soofivand, F., Tavakoli, F. (2012) Synthesis and characterization of copper ferrite nanocrystals via coprecipitation. *Journal of Cluster Science*, **23**(4), 1003–1010.

Salvatierra, R.V, Zitzer, G., Savu, S., Alves, A.P., Zarbin, A.J.G., Chassé, T., Casu, M.B., Rocco, M.L.M. (2015) Carbon nanotube/polyaniline nanocomposites: Electronic structure, doping level and morphology investigations. *Synthetic Metals*, **203**, 16–21.

Sang, C., Jin, S., Li, G., Luo, Y. (2021) Preparation of copper ferrite by sol–gel method and the synergistic catalytic for the thermal decomposition of ammonium perchlorate. *Journal of Sol-Gel Science and Technology*, **98**(3), 559–567.

Sathisha, I.C., Manjunatha, K., Bajorek, A., Rajesh Babu, B., Chethan, B., Ranjeth Kumar Reddy, T., Ravikiran, Y.T., Jagadeesha Angadi, V. (2020) Enhanced humidity sensing and magnetic properties of bismuth doped copper ferrites for humidity sensor applications. *Journal of Alloys and Compounds*, **848**, 156577. https://doi.org/10.1016/j.jallcom.2020.156577.

Science, E., Kumar, R.J. (2019) *Electrical Science & Engineering https://ojs.bilpublishing.com/index.php/ese ARTICLE*. **01**(01), 28–33.

Shai, Y. (2002) Mode of action of membrane active antimicrobial peptides, *Biopolymers*, 236–248. doi: 10.1002/bip.10260.

Shedam, R.M., Gadkari, A.B., Mathad, S.N., Shedam, M.R. (2016) Synthesis and Structural Investigation of Nano-Sized Cadmium Ferrite. *Journal of Modern Materials*, **2**(1), 7-12. https://doi.org/10.21467/jmm.2.1.7-12.

Sinfrônio, F.S.M., Rodrigues, J.A.O., Silva, F.C., Fonseca, R.S.P., de Menezes, A.S., Mouta, R., Sharma, S.K., Castro Junior, M.C. (2018) Effect of co-substitution on the vibrational, magnetic, and dielectric properties of copper ferrites obtained by microwave-assisted hydrothermal method. *Journal of Electronic Materials*, **47**(11), 6821–6832.

Strahl, H., Hamoen, L.W. (2010) Membrane potential is important for bacterial cell division. *Proceedings of the National Academy of Sciences of the United States of America*, **107**(27), 12281–12286.

Su, Y., Jiang, H., Zhu, Y., Yang, X., Shen, J., Zou, W., Chen, J., Li, C. (2014) Enriched graphitic N-doped carbon-supported Fe_3O_4 nanoparticles as efficient electrocatalysts for oxygen reduction reaction. *Journal of Materials Chemistry A*, **2**(20), 7281–7287.

Sundrarajan, M., Ramalakshmi, M. (2012) Novel cubic magnetite nanoparticle synthesis using room temperature ionic liquid. *E-Journal of Chemistry*, **9**(3), 1070–1076.

Tasca, J.E., Quincoces, C.E., Lavat, A., Alvarez, A.M., González, M.G. (2011) Preparation and characterization of $CuFe_2O_4$ bulk catalysts. *Ceramics International*, **37**(3), 803–812.

Wang, X., Gong, L., Zhang, D., Fan, X., Jin, Y., Guo, L. (2020) Room temperature ammonia gas sensor based on polyaniline/copper ferrite binary nanocomposites. *Sensors and Actuators, B: Chemical,* **322**, 128615. https://doi.org/10.1016/j.snb.2020.128615.

Wu, K., Saha, R., Su, D., Krishna, V.D., Liu, J., Cheeran, M. C.-J., Wang, J.-P. (2020) Magnetic immunoassays: A review of virus and pathogen detection before and amidst the *Coronavirus Disease-19 (COVID-19)*. **19**, 1–35.

Yao, Y., Lu, F., Zhu, Y., Wei, F., Liu, X., Lian, C., Wang, S. (2015) Magnetic core-shell $CuFe_2O_4$@ C_3N_4 hybrids for visible light photocatalysis of Orange II. *Journal of Hazardous Materials*, **297**, 224–233.

Yin, I.X., Zhang, J., Zhao, I.S., Mei, M.L., Li, Q., Chu, C.H. (2020) The antibacterial mechanism of silver nanoparticles and its application in dentistry, *International Journal of Nanomedicine*, **15**, 2555–2562.

Zakiyah, L.B., Saion, E., Al-Hada, N.M., Gharibshahi, E., Salem, A., Soltani, N., Gene, S. (2015) Up-scalable synthesis of size-controlled copper ferrite nanocrystals by thermal treatment method. *Materials Science in Semiconductor Processing*, **40**, 564–569.

Zeng, S., Yang, J., Qiu, X., Liang, Z., Zhang, Y. (2016) Magnetically recyclable $MnFe_2O_4$/polyaniline composite with enhanced visible light photocatalytic activity for rhodamine B degradation. *Journal of the Ceramic Society of Japan*, **124**(10), 1152–1156.

Zhang, W., Li, G., Chen, Y., Liu, S., Xu, J., Jing, C., Zhang, J., Yang, J., Cheng, Y., Chu, J. (2020) Dynamic liquid phase deposition of doped nanostructured PANI tube sensor for trace-level NH_3 gas detection. *Sensors and Actuators, B: Chemical*, **305**, 127459.

تشييد وتوصيف توليفات نانونيه من فريتات النحاس مع البولى-أنيلين وفاعليتها ضد الميكروبات

محمد على أحمد عيد[1]، عبير عبد الرحيم الهلالى[2]، محمد يسرى الشيخ [2]، حسنى احمد الدالى[2]، على حسن جميعى[2]

[1]قسم النبات والميكروبيولوجي- كلية العلوم – جامعة طنطا- طنطا- مصر، [2] قسم الكيمياء- كلية العلوم –جامعة طنطا- طنطا- مصر.

يعتبر تحميل التوليفات النانوية المغناطيسية بالعقاقير المضادة للميكروبات من الاتجاهات البحثيه الحديثه التي وجدت اهتماما متزيدا وذلك بسبب خصائصها المغناطيسية وقدرتها على إختراق الخلايا البكتيريه. كذلك من المعلوم جيدا أن أيونات النحاس تتميز بفاعليتها المضاده للميكروبات. في هذا البحث تم تشييد وتوصيف الجسميات النانوية من فريتات النحاس (ذات نسب مختلفة من أيون النحاس) $Cu_xFe_{3-x}O_4$ ثم دمجها مع البولي-أنيلين وبطريقة البلمرة المؤكسدة للانيلين باستخدام جسيمات فريتات النحاس $Cu_xFe_{3-x}O_4$ كعامل مؤكسد في وسط حمضي من خلال تقنية الوعاء الواحد لكى يتم الحصول على توليفات نانوية من فريتات النحاس / البولي-أنيلين $Cu_xFe_{3-x}O_4$ / PAN. ولقد تم التوصيف والتحقق من هذه التوليفات بالعديد من التقنيات مثل XRD، FT-IR، VSM، EDX, SEM و TEM و XPS والتى إثبتت وأكدت نجاح عملية التوليف. وعند قياس الخواص المغناطيسيه للعينات المحضرة إتضح زيادة خصائصها المغناطيسية الفائقة مع زيادة نسب أيون النحاسCu^{2+} سواء في حالة جسيمات الفريتات المفردة او تلك المدمجة مع البولي أنيلين. ولقد أظهر استخدام جسيمات فريتات النحاس وكذا التوليفات النانويه $Cu_xFe_{3-x}O_4$ / PAN تأثيرات إيجابيه مضادة للبكتريا موجبة الجرام مثل البكتيريا الكروية العنقودية الذهبية (*Staphylococcus aureus*)، سالبة الجرام مثل العصيات القولونية (*E. coli*) والزائفة الزنجارية (*Pseudomonas aeruginosa*) والكَلِبْسية الرئوية (*Klebsiella pneumoniae*) والفطريات مثل المُبيَضّة البيضاء (*Candida albicans*). وعند تفسير هذا التأثير الإيجابي المضاد للميكروبات اتضح انه يتوافق مع التناقص فى الحجم البلوري المقاس بوحدة النانومتر. كذلك وجد أن هناك علاقة عكسية بين الحجم البلوري والذي يتناقص مع زيادة نسبة +Cu2 في العينات المستخدمة. الاكثر من ذلك, فان الصور المجهرية SEM المأخوذه بأستخدام المجهر اللالكترونى الماسح كشفت عن وجود تغييرات في الشكل البكتيري ، وتشوه فى جدران الخلايا الفطرية وبالتالى انهيار المستعمرات البكتيرية والفطريه. علاوة على ذلك ، فإن التوليفات النانويه كانت أكثر فاعلية ضد البكتيريا سالبة الجرام مقارنة مع البكتريا موجبة الجرام. فى النهاية فإن نتائج هذه الدراسة تقدم نهجًا لاستخدام فريتات النحاس $Cu_xFe_{3-x}O_4$ والتوليفات النانونية لها مع البولي أنيلين $Cu_xFe_{3-x}O_4$ / PAN كبديل واعد مضاد للميكروبات المقاومة للعديد من الأدوية المعتمدة.